# nature communications



**Article** 

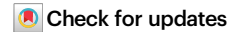
https://doi.org/10.1038/s41467-025-56417-5

# Orbital-order as the driving mechanism for superconductivity in ruthenates

Received: 10 April 2024

Accepted: 16 January 2025

Published online: 07 February 2025



Álvaro Adrián Carrasco Álvarez ® <sup>1,2</sup>, Sébastien Petit<sup>1</sup>, Wilfrid Prellier ® <sup>1</sup>, Manuel Bibes <sup>2</sup> & Julien Varignon ® <sup>1</sup>⊠

Several materials transition from an insulating to a superconducting state by reducing the strength of the electron-phonon coupling associated with charge and bond orderings provided that the coupling remains strong enough to produce Cooper pairs. While the Jahn-Teller effect is at the core of a strong electron-phonon coupling producing insulating states and orbital and bond orderings, its implication in superconductivity remains unobserved. Here, with parameter-free first-principles calculations, we reveal that superconductivity in  $A_2RuO_4$  (A = Sr, Ca) emerges due to an electron-phonon mechanism associated with the proximity of an orbital and bond-ordered phase. The model predicts critical temperatures  $T_c$  of 0.5–1.65 K in bulk  $Sr_2RuO_4$  and 63–73 K in pressured  $Ca_2RuO_4$ , in agreement with experiments. Our results suggest that phonons strongly coupled to electrons, such as those involved in charge disproportionation or Jahn-Teller effects and inducing band gaps in various oxides, could also serve as mediators of Cooper pairs in metallic phases.

Superconductivity (SC) is a peculiar property of materials characterized by no resistance to direct current and expulsion of magnetic fields, hence enabling many applications without energy loss. Yet, its practical implementation is limited by the low critical temperature T<sub>c</sub> reaching at best 135 K in the famous cuprates at ambient conditions<sup>1</sup>. SC is usually explained by the presence of bound electrons into Cooper pairs<sup>2</sup>. However, the origin of the attractive interaction between electrons still has to be understood and unified for all compounds. Among all superconductors, materials based on the  $A_{n+1}B_nO_{3n+1}$  Ruddlesden-Popper structure attract the largest interest of solid-state physicists and chemists (Fig. 1a for n=1). These structures are based on corner-sharing O<sub>6</sub> groups centered on B cations, forming a building ABO<sub>3</sub> perovskite block. Then, n perovskite blocks are stacked along the c-axis and are separated by a spacing AO layer. This generic structure hosts most oxide superconductors, entailing cuprates<sup>1</sup> and ruthenates<sup>3</sup> (La<sub>2-x</sub>Sr<sub>x</sub>CuO<sub>4</sub> and  $Sr_2RuO_4$ , n=1 member), antimonates<sup>4</sup> and bismuthates<sup>5,6</sup> (Ba<sub>1</sub>- $_{x}K_{x}SbO_{3}$ ,  $Ba_{1-x}K_{x}Bi_{1-y}Pb_{y}O_{3}$ ,  $n = \infty$  members) and nickelates<sup>7-9</sup> under high pressures (La<sub>3</sub>Ni<sub>2</sub>O<sub>7</sub>, n = 2) or after a chemical reduction aiming at removing apical oxygen (Nd<sub>6</sub>Ni<sub>5</sub>O<sub>12</sub>, n = 5 member, or R<sub>1-x</sub>A<sub>x</sub>NiO<sub>2</sub>,  $n = \infty$  with R=La, Pr or Nd and A = Ca or Sr).

Interestingly, bismuthates, antimonates, and some nickelates are superconductors due to an electron-phonon mechanism related to a charge and bond ordering (CBO)<sup>10-14</sup>, whose origin is the existence of an unstable formal oxidation state  $\delta$  (FOS) of B cations in the doping phase diagram. It produces a rock salt pattern of  $B^{(\delta+1)+}$  and  $B^{(\delta-1)+}$ cations and hence a charge ordering. It is accompanied by a bond disproportionation Boc mode producing a bond ordering (BO). It thus presents a strong electron-phonon coupling (EPC) and is able to produce an insulating phase (see Supplementary Note 1). Starting from this CBO-insulating phase, doping the materials weakens the EPC and produces a metal without any stable CBO. However, this does not imply that the BO mode is not coupled to the electronic structure, since the EPC remains sufficiently large to produce an attractive interaction that binds electrons into Cooper pairs. This mechanism is also at the core of SC in many other non-oxide materials<sup>15-18</sup>, showing that the same phonon can be responsible for the insulating and superconducting state in the doping phase diagram.

Nonetheless, the CBO mode is not the only phonon that can produce an insulating phase in oxides. The other type of phonon is the one associated with the Jahn-Teller effect (JTE) and its related Jahn-Teller distortion (JTD)<sup>19,20</sup> (see Supplementary Note 1). According to

<sup>1</sup>Laboratoire CRISMAT, ENSICAEN, CNRS, Université de Caen, Normandie Université, Caen, France. <sup>2</sup>Laboratoire Albert Fert—CNRS, Thales, Université Paris Saclay, Palaiseau, France. ⊠ e-mail: julien.varignon@ensicaen.fr

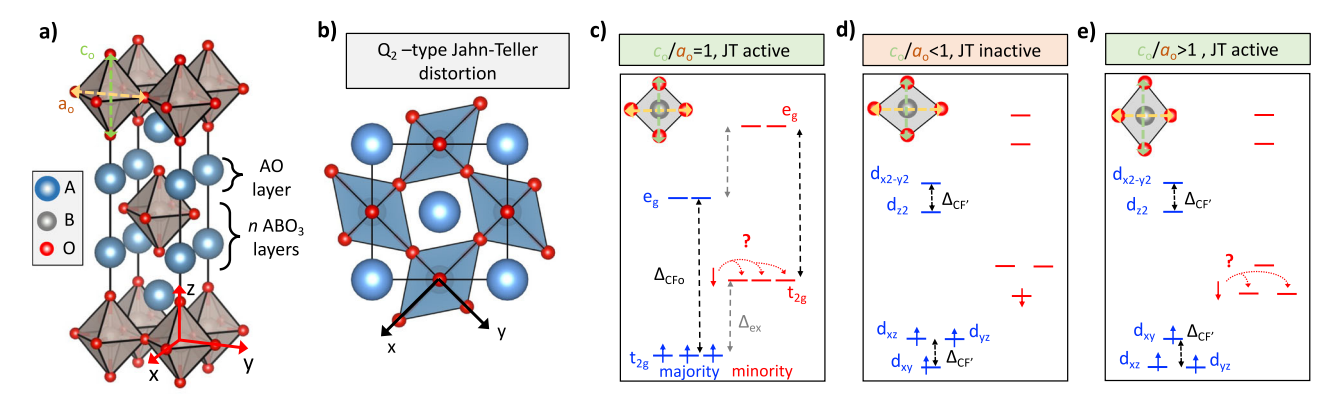


Fig. 1 | Structural and electronic features exhibited by ruthenates  $A_2RuO_4$ . a Crystallographic structure exhibited by n=1 undistorted Ruddlesden-Popper phase. The undistorted cell adopts an I4/mmm symmetry based on ABO $_3$  perovskite building blocks stacked along c and separated by one AO layer. b Jahn-Teller distortion for one ABO $_3$  layer, corresponding to a  $Q_2$  mode, producing a contraction and elongation of two B-O bond lengths with alternating contraction/expansion on nearest neighbor B sites.  $\mathbf{c}-\mathbf{e}$  Ru d states splitting according to  $O_6$ 

octahedral deformations for totally undistorted  $O_6$  groups (**c**), compressed (**d**), or extended (**e**). The distortion is determined by the  $c_0$  and  $a_0$  ratios defined in (**a**).  $\Delta_{\text{CFo}}$  and  $\Delta_{\text{ex}}$  are octahedral crystal fields and exchange splitting, respectively. Majority (minority) spin channel is represented in blue (red). The point group symmetry for the undistorted octahedral situation is  $O_h$ , that can be lowered to  $D_{2h}$  by a  $c_0/a_0 \neq 1$  and produce an additional  $\Delta_{\text{CF}}$  splitting.

the Jahn and Teller theorem, a degenerate electronic configuration, such as one electron for two or three degenerate orbitals, is unstable and can produce a lattice distortion that breaks the degeneracy<sup>21</sup>. The JTE then produces occupancy of alternating orbitals between all nearest neighbor B sites, leading to an orbital-ordering (OO). It is accompanied by a so-called Jahn-Teller distortion (JTD)<sup>20</sup> deforming octahedra in order to accommodate the OO. Hence, it yields electron localization and can produce an insulating state (Supplementary Note 1). Famous examples fulfilling all modalities for a JTE are KCuF<sub>3</sub> or RVO<sub>3</sub> (R = Lu-La, Y)<sup>20,22,23</sup>.

The presence of a degenerate electronic configuration is a prerequisite but not a sufficient condition for a JTE (or disproportionation effects)<sup>14,20,24</sup>: if the electronic structure is too hybridized, the electronic instability at the core of the JTE is screened, and it cannot enforce an OO and ensuing JTD. In view of the similarity to the situation of SC mediated by charge and bond ordering distortions, it is natural to ask if the JTE and its resulting JTD and OO could produce a SC transition in a metallic compound and if there are any materials that sit in the vicinity of an orbital-ordered phase. To the best of our knowledge, this remains elusive.

Good candidates for a JTE are the ruthenates  $A_2RuO_4$  (A = Ca, Sr). These compounds are n = 1 members of the RP series with Ru<sup>4+</sup> cations in a d<sup>4</sup> electronic configuration<sup>25,26</sup>. The octahedral crystal field (CF)  $\Delta_{CFo}$  is greater than the exchange splitting  $\Delta_{ex}$  and lifts the d orbital degeneracy in two groups of degenerate partners (Fig. 1c). Consequently,  $Ru^{4+}$  cations are in a  $t_{2g,\uparrow}{}^3t_{2g,\downarrow}{}^1$  electronic configuration that is nominally Jahn-Teller active. Nevertheless, due to the A-to-Ru cation size mismatch, Ca<sub>2</sub>RuO<sub>4</sub> and Sr<sub>2</sub>RuO<sub>4</sub> distort from the I4/mmm cells with equivalent  $c_0$  and  $a_0$  Ru-O bond length in  $O_6$  groups (see Fig. 1a) to a distorted cell with distinct  $c_o$  and  $a_o$  values. Ca<sub>2</sub>RuO<sub>4</sub> adopts a Pbca symmetry<sup>25</sup> characterized by a a c<sup>+</sup> octahedral rotations in Glazer's notation<sup>27</sup> and a  $c_0/a_0$  ratio lower than 1 ( $c_0/a_0$  = 0.981, see Table 1). The local symmetry breaking induced by steric effects produces an additional CF  $\Delta_{CF}$  lifting the degeneracy of  $t_{2g}$  levels, stabilizing the  $d_{xy}$ orbital over the d<sub>xz</sub>/d<sub>yz</sub> doublet (Fig. 1d). It allows the electron localization in the  $d_{xy}$  orbital in the minority spin channel and thus a band gap opens. It explains the insulating state of Ca<sub>2</sub>RuO<sub>4</sub> below 357 K<sup>19,28,29</sup> with a band gap of at least 0.4 eV30. In contrast, Sr2RuO4 adopts an elongated I4/mmm cell at  $300K^{26}$  inducing a  $c_0$  parameter greater than  $a_0$  ( $c_0/a_0 = 1.069$ , Table 1) and thus here  $\Delta_{CF}$  stabilizes the  $d_{xz}/d_{yz}$ doublet over the  $d_{xy}$  orbital. One is then left with a single electron for two degenerate orbitals in the minority spin channel (Fig. 1e). Although possessing the precursor to a ITE, Sr<sub>2</sub>RuO<sub>4</sub> is metallic and

superconducting with a critical temperature  $T_{\rm c}$  of roughly 1.5 K<sup>3,31</sup>. Fulfilling the condition for a JTE, Sr<sub>2</sub>RuO<sub>4</sub> is a potential candidate for exhibiting SC at the vicinity of an OO phase with an EPC mediated by the subsequent JTD.

In this article, using parameter-free Density Functional Theory (DFT) calculations, we reveal that  $\rm Sr_2RuO_4$  is intrinsically in the vicinity of a Jahn-Teller effect due to a hybridized electronic structure. Then, an electron-phonon coupling (EPC) associated with the related Jahn-Teller distortion explains the  $T_c$  observed experimentally. The model further reproduces a superconducting state in  $\rm Ca_2RuO_4$  nanofilms with a  $T_c$  of 63–73 K compatible with the experimental value oscillating between 64 or 80 K $^{32}$ . Thus, superconductivity in oxides with partly filled d states might be given by the same electron-phonon interactions that produce the insulating phases $^{19}$ .

#### Results

We first perform the structural relaxation (atomic positions plus cell parameters) of bulk Ca<sub>2</sub>RuO<sub>4</sub> and Sr<sub>2</sub>RuO<sub>4</sub> considering several magnetic solutions. Table 1 reports the relevant structural parameters as well as the gap amplitude and Ru magnetic moments. Firstly, the non-magnetic (NM) solution is metallic and at least 84 meV/f.u (i.e., 1000 K/f.u) above any spin-polarized solutions for the two compounds. It highlights that the NM approximation is not suitable to describe the properties of ruthenates. Using spinpolarized solutions, Ca<sub>2</sub>RuO<sub>4</sub> is a C-type antiferromagnet (AFM-C) insulator in the ground state with a gap  $E_{\rm g}$  of 0.574 eV, in agreement with experimental results showing an AFM transition at 110 K and a band gap greater than 0.4 eV<sup>30,33</sup> (Fig. 2a). The gap is formed between occupied  $d_{xy}$  and unoccupied  $d_{xz}/d_{yz}$  orbitals due to a computed  $c_o/a_o$  ratio lower than one as anticipated in Fig. 1d. In contrast to Ca<sub>2</sub>RuO<sub>4</sub>, Sr<sub>2</sub>RuO<sub>4</sub> is metallic with ferromagnetic (FM) interactions between Ru cations, compatible with experimental reports suggesting the presence of short-range FM order<sup>34</sup> and metalicity<sup>3</sup>. Furthermore, the  $d_{xz}$  and  $d_{yz}$  orbitals mostly contribute to states at the Fermi level  $E_F$ , in agreement with the situation for a computed  $c_0/a_0$  ratio greater than one displayed on Fig. 1e. In both compounds, the computed magnetic moments,  $m = 1.413 \,\mu_B/\text{Ru}$  and  $m = 1.364 \mu_B/Ru$  in Ca<sub>2</sub>RuO<sub>4</sub> and Sr<sub>2</sub>RuO<sub>4</sub>, respectively, are compatible with a Ru<sup>4+</sup> cations in a low spin state  $(t_{2g\uparrow}^3 t_{2g\downarrow}^1, S=1)$  albeit the amplitudes deviate from the expected value of 2 µ<sub>B</sub>/Ru. This discrepancy originates from a hybridized electronic structure between Ru-d and O-p states producing spillage of magnetic moments on surroundings O anions (Fig. 2). The values are however in

Table 1	Key pro	perties of A	A <sub>2</sub> RuO <sub>4</sub>	compounds
---------	---------	--------------	---------------------------------	-----------

	Ca <sub>2</sub> RuO <sub>4</sub>						Sr <sub>2</sub> RuO <sub>4</sub>								
Mag.	Space group	ΔΕ (meV/ RuO <sub>3</sub> )	c <sub>o</sub> /a <sub>o</sub>	m (µ <sub>в</sub> )	E <sub>g</sub> (eV)	Q <sub>JTD</sub> (Å/f.u)	Q a˙a˙c <sup>o</sup> (Å/f.u)	Q aºaºc⁺ (Å/f.u)	Space group	ΔΕ (meV / RuO <sub>3</sub> )	c <sub>o</sub> /a <sub>o</sub>	т (µ <sub>В</sub> )	E <sub>g</sub> (eV)	Q <sub>JTD</sub> (Å/f.u)	Q aºaºc⁺ (Å/f.u)
NM	Pbca	0	1.064	-	0	0	0.469	0.558	Cmca	0	1.080	-	0	0	0.005
FM	Pbca	-299	0.984	1.430	0.104	0.023	0.767	0.542	Cmca	-180	1.057	1.364	0	0	0.365
AFM-A	Pbca	-300	0.981	1.425	0.161	0.023	0.768	0.543	Cmca	-178	1.057	1.364	0	0	0.372
AFM-C	Pbca	-302	0.963	1.413	0.574	0.031	0.745	0.590	Pbam	-84	1.065	1.151	0.120	0.044	0.048
PM	P-1	-299	0.967	1.410	0.500	0.031	0.755	0.582	Pm	-142	1.036	1.258	0	0	0.080
Exp.	Pbca (180 K) <sup>25</sup>	_	0.981 <sup>25</sup>	1.30 <sup>33</sup>	>0.4 <sup>30</sup>	0.011	0.683	0.562	14/mmm (300 K) <sup>26</sup>	_	1.069 <sup>26</sup>	-	Met. <sup>3</sup>	0	0

Energy difference  $\Delta E$  (in meV/RuO<sub>3</sub> motif) between spin-polarized and the non-spin polarized NM solution. Average magnetic moments m exhibited by Ru cations (in  $\mu_B$ ) as well as band gaps Eg (in eV) are reported. The key structural parameters reflected by the  $c_0/a_0$  ratio quantifying the octahedral deformation as well as the amplitude Q of the Jahn-Teller  $Q_2$ -type distortion and  $a^a a^a c^+$  and  $a^a a^a c^+$  octahedral rotation (in A/f.u) are provided. JTD and rotations amplitude are extracted by considering only a single block of perovskites along the c-axis in order to avoid folding of zone boundary modes during the analysis.

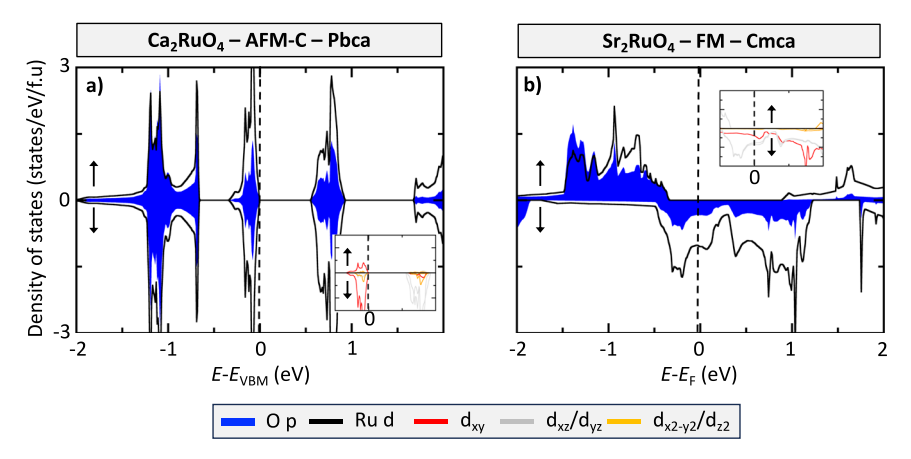


**Fig. 2** | **Electronic structure of Ca<sub>2</sub>RuO<sub>4</sub> and Sr<sub>2</sub>RuO<sub>4</sub> ground states.** Density of states (in states/eV/f.u) for spin up (positive values) and spin down (negative values) channels as a function of the energy (in eV) projected on Ru d (black line) and O p (blue filled area) states for Ca<sub>2</sub>RuO<sub>4</sub> (a) and Sr<sub>2</sub>RuO<sub>4</sub> (b) ground states. Projection

on  $d_{xy}$  (red line),  $d_{xz}$  and  $d_{yz}$  (grey line), and  $d_{x^2,y}^2$  and  $d_z^2$  (orange line) orbitals around the valence and maximum is provided as inserts. The AFM-C and FM orders are used for  $Ca_2RuO_4$  and  $Sr_2RuO_4$ , respectively. The black dashed vertical line represents the valence band maximum or the Fermi level.

agreement with the experimental value of 1.3  $\mu_B$  in Ca<sub>2</sub>RuO<sub>4</sub><sup>33</sup> and previously computed to 1.38  $\mu_B$  in Sr<sub>2</sub>RuO<sub>4</sub><sup>35</sup>.

The structural relaxations correctly predict the Pbca space group for all spin-polarized solutions with an a<sup>-</sup>a<sup>-</sup>c<sup>+</sup> octahedral rotation pattern in Ca<sub>2</sub>RuO<sub>4</sub>, with amplitudes of distortions in agreement with experimental data available in literature<sup>25</sup> (Table 1), at the exception of the PM order. The lower symmetry exhibited by the PM phase is explained by the introduced spin disorder in our simulations that removes symmetry operations (see methods). Nevertheless, the relaxed structure is still characterized by the a-a-c+ octahedral rotations with amplitudes compatible with experiments. In Sr<sub>2</sub>RuO<sub>4</sub>, we identify that the OK relaxed structure adopts a Cmca space group characterized by a<sup>0</sup>a<sup>0</sup>c<sup>+</sup> O<sub>6</sub> groups rotation for all magnetic orders at the exception of AFM-C (Pbam) and PM (Pm) orders that have lower space groups. The Cmca contrasts with the I4/mmm cell proposed experimentally<sup>26</sup>. However, the experimental structure is obtained at 300 K, and no structures at low temperatures are reported so far for Sr<sub>2</sub>RuO<sub>4</sub> to the best of our knowledge, hindering the comparison with our first-principles 0 K structure. The lower symmetry exhibited by the DFT-PM relaxation of Sr<sub>2</sub>RuO<sub>4</sub> is again explained by the disorder introduced on the spin-ordering. The Pbam symmetry, a lower space group to Cmca, exhibited by the AFM-C order is discussed below.

The correct trend of  $c_0/a_0$  ratio is obtained from the DFT simulations with respect to experiments for  $Ca_2RuO_4$  and  $Sr_2RuO_4$  regardless of the imposed magnetic order with the exception of the

NM solution in Ca<sub>2</sub>RuO<sub>4</sub>. In Ca<sub>2</sub>RuO<sub>4</sub>, the  $c_0/a_0$  ratio is lower than one and yields an insulating state whatever the spin-polarized solution. In contrast, although the  $c_0/a_0$  is greater than 1, whatever the spin orderings in Sr<sub>2</sub>RuO<sub>4</sub>, all magnetic orders yield a metal except the AFM-C order, which produces a gap  $E_{\rm g}$  of 0.1 eV. Using a symmetry mode analysis of the relaxed structure with respect to a high symmetry undistorted I4/mmm cell, we observe a sizable Jahn-Teller distortion only for the AFM-C order. It corresponds to a Q<sub>2</sub>-type mode with two Ru-O bond lengths contraction and extension, alternating on neighboring octahedra<sup>20,36-38</sup> (see Fig. 1b). Ca<sub>2</sub>RuO<sub>4</sub> also exhibits a non-zero ITD but for all magnetic orders. However, this is simply a consequence of a coupling between the JTD and the a a c type of octahedral rotations in Glazer's notations<sup>27</sup> and hence this JTD has an improper origin rather than a proper, electronic, origin (see Supplementary Note 2). Nevertheless, the absence of the appropriate octahedral rotations in Sr<sub>2</sub>RuO<sub>4</sub> cannot explain its appearance only for the AFM-C order. Hence, a degeneracy of these two orbitals exists in Sr<sub>2</sub>RuO<sub>4</sub>.

In order to understand the appearance or not of a Jahn-Teller mode as a function of the magnetic orders in  $Sr_2RuO_4$ , we report on Fig. 3a the potential energy surface associated with the JTD for a NM, FM, and AFM-C solutions. To that end, we start from a perfectly undistorted cell of  $Sr_2RuO_4$  with I4/mmm symmetry and freeze-in some amplitudes Q of the JTD. For the NM and FM solutions, we observe a single well potential whose minimum is located at  $Q_{\rm JTD} = 0$ . Therefore, the Jahn-Teller mode is not willing to appear in the material.

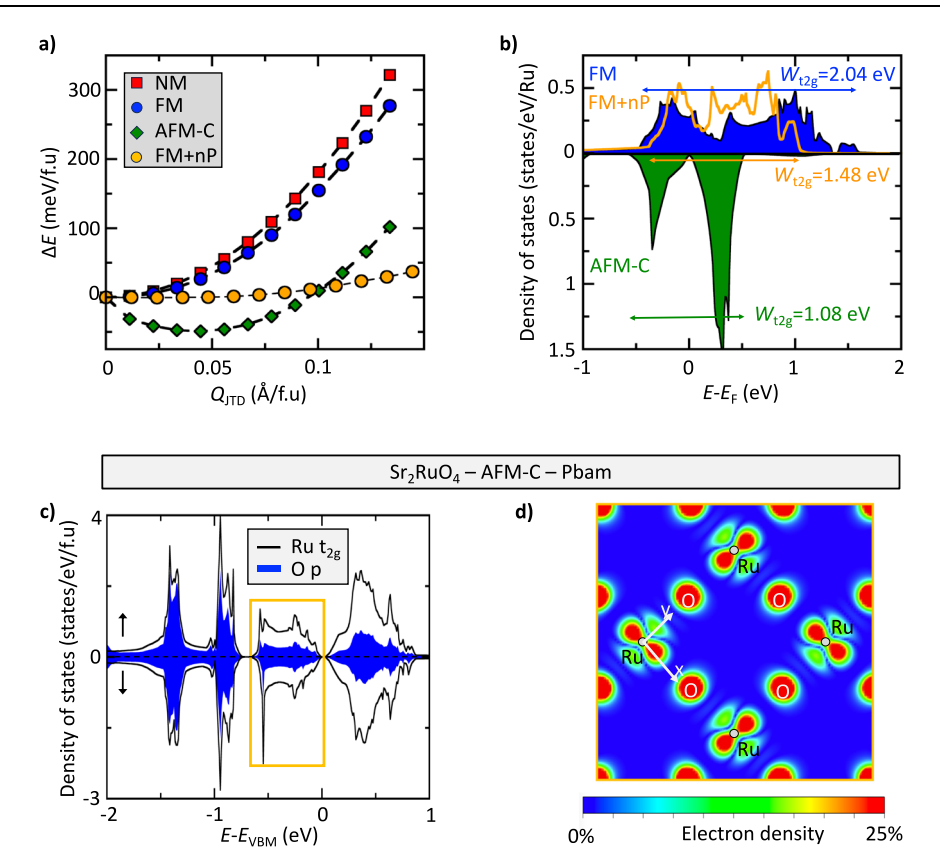


**Fig. 3** | **Jahn-Teller effect in Sr<sub>2</sub>RuO<sub>4</sub>. a** Energy gain  $\Delta E$  (in mev/f.u) associated with the condensation of different amplitude  $Q_{\rm JTD}$  (in Å/f.u) of the  $Q_2$ -type JTD in Sr<sub>2</sub>RuO<sub>4</sub> for the NM (red filled squares), FM (blue filled circles), AFM-C (green filled diamonds) and FM with a negative Pressure (FM-nP, orange filled circles) starting from an undistorted I4/mmm cell. **b** Density of states of Ru t<sub>2g</sub> states in the minority spin channel for the FM (upper part, blue filled area), FM + negative pressure (upper part, green line), and AFM-C order (lower panel, green filled area) within a totally

undistorted I4/mmm cell.  ${\bf c}$  Density of states (in states/eV/f.u) for spin up (positive values) and spin down (negative values) channels as a function of the energy (in eV) projected on Ru  $t_{2g}$  (black line) and O p (blue filled area) states in  $Sr_2RuO_4$  ground state with the AFM-C order.  ${\bf d}$  Partial charge density map associated with states around the Fermi level indicated by the orange area in ( ${\bf c}$ ) for  $Sr_2RuO_4$  with the AFM-C order.

However, a shifted single well potential for the AFM-C order whose minimum is at  $Q_{\rm ITD} \neq 0$  is observed with an energy gain of -49 meV/f.u with respect to the high symmetry I4/mmm cell. This signals the presence of an electronic instability associated with a single electron for two degenerate partners. Should the material be characterized by dominant AFM interactions,  $Sr_2RuO_4$  would thus exhibit a Jahn-Teller effect, producing an insulating orbital ordered phase accompanied by a JTD with the Ru d electron in the minority spin channel located either in the  $d_{xz}$  or  $d_{yz}$  orbital on alternating first-nearest neighbors (see Fig. 3c and d). The lower Pbam symmetry observed for the AFM-C order in  $Sr_2RuO_4$  with respect to all other spin-polarized solutions is related to a structural symmetry breaking induced by the JTE and ensuing JTD. It produces a band gap  $E_{\rm g}$  of 0.12 eV (Table 1).

The discrepancy between FM and AFM-C orders can be understood by their different electronic structures. We report on Fig. 3b the projected density of states Ru  $t_{2g}$  states in the minority spin channel in the high symmetry I4/mmm cells for FM and AFM-C orders. These two magnetic orders are characterized by very distinct bandwidth  $W_{t2g}$  associated with  $t_{2g}$  levels, estimated to 2.04 eV and 1.08 eV for FM and AFM-C orders, respectively. Recalling that (i) electronic instabilities strongly depend on bandwidth—i.e., localized states/correlation strength— and (ii) that AFM orders improve band compacities 14,20,24, the AFM-C order preserves the electronic instability toward JTE while it is screened with an FM order. This is confirmed by performing a calculation of the JTD potential with an FM order in which the Ru d states band compacity is improved by increasing the lattice parameters by 8%, thus creating a negative

pressure effect (FM-nP,  $W_{\rm t2g}$  = 1.48 eV, Fig. 3b) that yields a strong softening of the JTD potential (Fig. 3a). A DFT + U scheme with a U potential on Ru d states preventing electron delocalization leads to the very same conclusion (see Supplementary Note 3). Hybridizations were recently observed to have a similar role on disproportionation effects<sup>14</sup>. We conclude here that  $\rm Sr_2RuO_4$  is intrinsically at the vicinity of a JTE and subsequent orbital-ordered phase.

We report in Fig. 4a the band structure unfolded to the primitive I4/mmm cell of  $Sr_2RuO_4$  in the FM ground state with a Cmca symmetry. The majority spin channel is gapped between occupied  $t_{2g}$  and unoccupied  $e_g$  states, as expected for a half-filled electronic configuration  $^{19}$ . In the minority spin channel, three bands cross the Fermi level with (i) a parabola centered at the  $\Gamma$  point dispersing on roughly 3.52 eV with a dominant  $d_{xy}$  character and (ii) two degenerate bands dominated by the  $d_{xz}$  and  $d_{yz}$  orbitals but dispersing only on 1.72 eV. No energy gaps are observed in the band dispersion, indicating that electrons are not experiencing interactions from the lattice.

Although the EPC associated with the JTD is not strong enough to drive a metal-insulator transition with localization of electrons, it is straightforward to ask if the EPC can remain sufficiently large to mediate the Cooper pairs formation in  $Sr_2RuO_4$ . To that end, we evaluate the electron phonon-coupling constant  $\lambda$  associated with the JTD  $Q_2$ -type mode through the following formula<sup>39</sup>  $\lambda = N(E_F) \frac{\hbar^2}{2M\omega_{PTD}^2} D^2$  where  $N(E_F)$  is the density of states at the Fermi level  $E_F$  associated with a band,  $\omega_{JTD}$  is the frequency of the JTD, M is the mass of the moving atoms (O in the present situation) and D is the reduced electron-

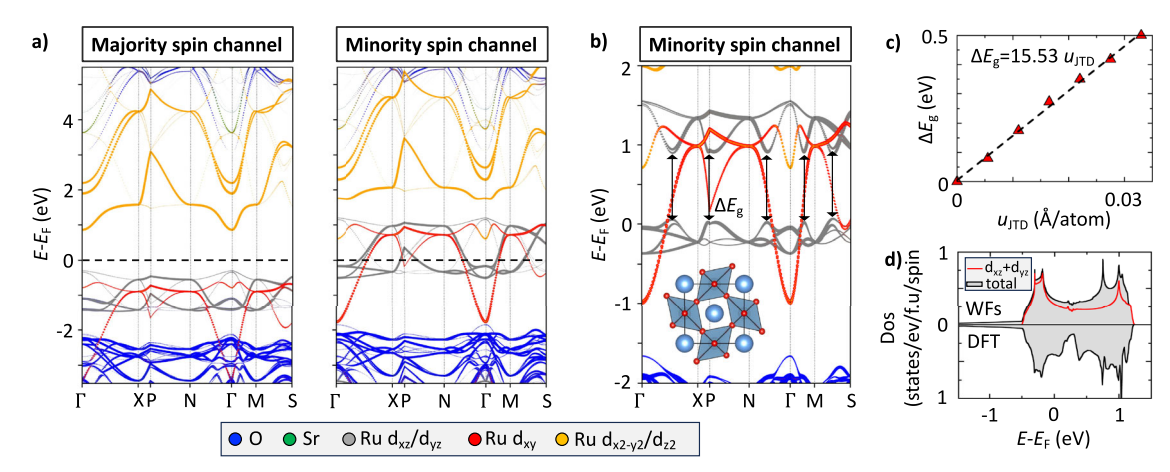


**Fig. 4** | **Band structure of Sr<sub>2</sub>RuO<sub>4</sub> superconductors.** a Band structure of the FM ground state of Sr<sub>2</sub>RuO<sub>4</sub> (Cmca symmetry) unfolded to primitive I4/mmm cell and projected on O (blue), Sr (green), Ru  $d_{xy}$  (red),  $d_{xz}$ + $d_{yz}$  (grey) and  $d_x^2$ - $y^2$  and  $d_z^2$  (orange) states. Majority (left panel) and minority (right panel) are reported. **b** Band splitting  $\Delta E_g$  induced by freezing a displacement  $u_{JTD}$  of 0.066 Å/atom associated with the JTD  $Q_2$ -type mode in Sr<sub>2</sub>RuO<sub>4</sub> ground state. **c** Evolution of  $\Delta E_g$  as a function of the displacement  $u_{JTD}$  (Å per atom) associated with the JTD  $Q_2$ -type mode. The

computed REPME is D=7.76 eV. Å $^{-1}$ . **d** Total density of states (in states/eV/f.u/spin, grey area) as a function of the energy using the DFT calculation (lower part) and atomic-like Wannier functions (upper part). The WFs allow to extract the contributions from the sole  $d_{xz}$  and  $d_{yz}$  orbitals (red line). The contribution from each  $d_{xz}$  or  $d_{yz}$  band is then of  $N(E_F)=0.291$  states/eV/Ru/spin/band. The k-mesh is sampled with 12x12x4 points for the DFT calculation and with 256x256x64 points for the WFs.

phonon matrix element (REPME) quantifying the change in the electronic structure according to a vibration (see methods).

The frequency of the JTD mode is computed by a frozen displacement approach and yields a value of 81 meV (see methods and Supplementary Note 4). The condensation of the ITD in the ground state structure produces band splitting near  $E_F$  along the  $\Gamma$  – X,  $\Gamma$  – N,  $\Gamma$  – M, and M - S path for the two bands involving the  $d_{xz}$  and  $d_{yz}$  orbitals (Fig. 4b). We have computed D for different  $u_{\text{ITD}}$  values and we observe a linear response between  $\Delta E_{\rm g}$  and  $u_{\rm ITD}$ . Through a linear fit of the  $\Delta E_{\rm g}$  vs.  $u_{\rm ITD}$  curve, we extract an average D of 7.76 eV.Å<sup>-1</sup>. In order to extract the density of states (dos) at  $E_{\rm E}$  for these two contributing bands, we have built the Wannier Functions (WFs) associated with the minority spin channel aiming to extract atomic like WFs with dxy, dxz and dyz characters centered on Ru cations (see methods and Supplementary Note 5). It further allows to converge the dos on a very fine kmesh and extracts contribution from bands altered by the JTD-i.e., d<sub>xz</sub> and d<sub>vz</sub>. We end up with  $N(E_{\rm F}) = 0.2908$  states/eV/f.u/spin for both  $d_{\rm xz}$  and  $d_{\rm yz}$  bands. Using these quantities, we obtain an EPC of  $\lambda = 0.35$  yielding a  $T_c$  oscillating between 1.65 K and 0.5 K for usual screened Coulomb potential µ\* of 0.1 and 0.15, respectively. This value is reminiscent of the experimental  $T_c$  of ~1.5 K. We emphasize that the calculation of  $\lambda$  with a non-spin polarized solution (NM) yields a lower value of  $\lambda = 0.08$  due to (i) an intrinsic underestimation D to 3.56 eV.Å<sup>-1</sup> and (ii) a hardening of the JTD to 98 meV (Supplementary Note 6). However, it is now well known that NM underestimates and/or fails at predicting bands splitting and entangled electron-phonon features by neglecting the basic Hund's rule<sup>12,19</sup>. We have checked that the spin-orbit interaction has marginal effects on the electronic properties and we identify that the EPC is unchanged (see Supplementary Note 7). We have finally tested other type of Jahn-Teller distortion that could be observed in other materials such as the Q<sub>3</sub> distortion<sup>36</sup> with planar Ru-O bond length contraction and out of plane Ru-O bond length elongation, with opposite motion on neighboring Ru sites (see Supplementary Note 8). This JTD Q<sub>3</sub>-type mode is identified to have a negligible coupling to the electronic structure (of  $\lambda$  = 0.14) and hence cannot bind electrons into Cooper pairs.

A recent study revealed a possible SC state with a  $T_{\rm c}$  of roughly 64 K coexisting with ferromagnetism in Ca<sub>2</sub>RuO<sub>4</sub> nanofilm single crystals<sup>32</sup>. The nanofilm corresponds to a pressured materials allowing to tune the  $c_{\rm o}/a_{\rm o}$  ratio. The consequential effect is to restore the vicinity of a JTE in Ca<sub>2</sub>RuO<sub>4</sub> for  $c_{\rm o}/a_{\rm o} > 1$ . We performed additional DFT simulations on Ca<sub>2</sub>RuO<sub>4</sub> by using the lattice

parameter of Ref. 32 (i.e., a = 5.343 Å, b = 5.350 Å and c = 12.778 Å). We then perform the relaxation of atomic positions at fixed lattice parameters. We end up with a Pbca symmetry similar to the bulk but with a  $c_0/a_0$  ratio of 1.05 and the material is found metallic with a FM order. Thus, the JTE is screened in the Ca<sub>2</sub>RuO<sub>4</sub> nanofilms in the spirit of Sr<sub>2</sub>RuO<sub>4</sub> bulk compounds. Following the very same procedure as in Sr<sub>2</sub>RuO<sub>4</sub> with the same JTD Q<sub>2</sub> -type mode, the EPC is computed to 1.68, yielding a  $T_c$  between 73 and 63 K for  $\mu^*$  of 0.1 and 0.15, respectively (see Fig. 5). It hints at the experimental value with a possible  $T_c = 64$  K<sup>32</sup>, thereby confirming the model proposed to explain SC in bulk Sr<sub>7</sub>RuO<sub>4</sub>.

Ca<sub>2</sub>RuO<sub>4</sub> under pressure and Sr<sub>2</sub>RuO<sub>4</sub> bulk possess the same root underpinning superconductivity. Nevertheless, the EPC is much larger in  $Ca_2RuO_4$  ( $\lambda = 1.68$ ) than in  $Sr_2RuO_4$  ( $\lambda = 0.35$ ). At odds with  $Sr_2RuO_4$ ,  $Ca_2RuO_4$  as a nanofilm material retains its  $a^-a^-c^0$  (labeled  $\phi^-$ ) and  $a^0a^0c^+$  (labeled  $\phi^+$ ) octahedral rotations with amplitudes  $Q_{\phi^-}$  = 0.639 Å/f.u and  $Q_{\phi^+}$  = 0.479 Å/f.u. By means of a free energy expansion associated with the amplitude of the JTD Q2 -type mode and octahedral rotations  $\phi^-$  and  $\phi^+$ , we identify interesting couplings between the biquadratic term of JTD  $Q_2$  -type mode with the rotations:  $F \propto$  $(a_{20} + a_{22}Q_{\phi}^2)Q_{JTD}^2 \propto a_{eff}Q_{JTD}^2$  where  $a_{20}$  and  $a_{22}$  are coefficients. Recalling that the energy of a harmonic oscillator is  $E = \frac{1}{2}M\omega_{\text{ITD}}^2Q_{\text{ITD}}^2$ , we get that  $\omega_{\text{ITD}} = \sqrt{\frac{2a_{\text{eff}}}{M}}$ . Therefore, it follows that the frequency of the JTD mode can be altered by the presence of octahedral rotations. This is confirmed in our simulations in which octahedral rotations produce a renormalization of the frequency of the JTD to 46 meV in the ground state instead of 100 meV in a phase without any octahedral rotation (see methods and Supplementary Note 9). This observation is very similar to the strong softening of the bond disproportionation (BO) frequency with octahedral rotations amplitude appearing in rare-earth nickelates and bismuthates<sup>10,40</sup>.

The resulting REPME in  $Ca_2RuO_4$  is evaluated to  $D=9.55 \text{ eV.Å}^{-1}$  without  $O_6$  groups rotation and to  $D=8.77 \text{ eV.Å}^{-1}$  with octahedral rotations, a value roughly matching that of  $Sr_2RuO_4$ . The density of states at the Fermi level  $N(E_F)$  associated with the  $d_{xz}$  and  $d_{yz}$  orbitals remains very similar, with  $N(E_F)=0.31$  states/eV/f.u/spin/band vs  $N(E_F)=0.29$  states/eV/f.u/spin/band in  $Ca_2RuO_4$  and  $Sr_2RuO_4$ , respectively. Thus the strong softening of the JTD in  $Ca_2RuO_4$  yields an EPC of 1.68. The presence of octahedral rotations with strongly coupled electron-phonon features is thus a potential lever for tuning the superconducting properties of oxide materials.

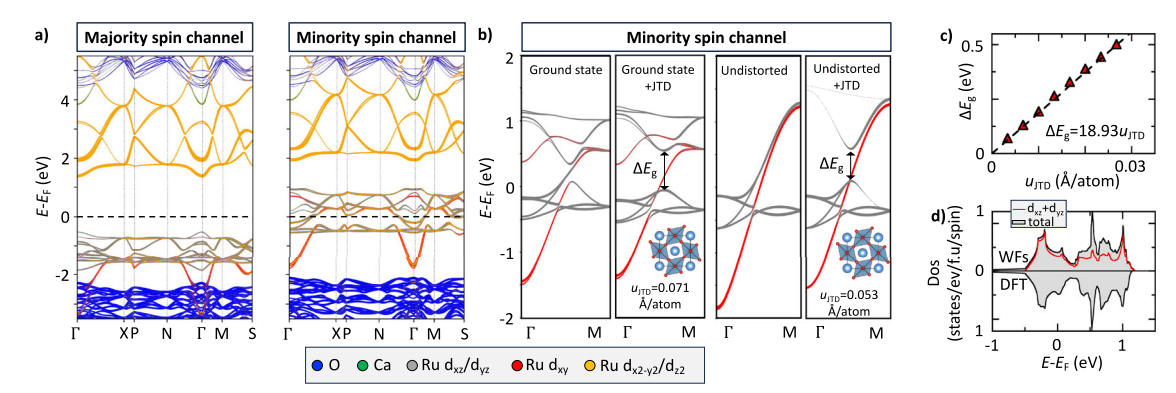


**Fig. 5** | **Superconducting properties of Ca<sub>2</sub>RuO<sub>4</sub> as a nanofilm. a** Band structure of Ca<sub>2</sub>RuO<sub>4</sub> as a nanofilm using a FM order unfolded to primitive I4/mmm cell and projected on O (blue), Ca (green), Ru  $d_{xy}$  (red),  $d_{xz}+d_{yz}$  (grey) and  $d_x^2$ - $y^2$  and  $d_z^2$  (orange) states. Majority (left panel) and minority (right panel) are reported. **b** Band splitting  $\Delta E_g$  induced by freezing a displacement  $u_{JTD}$  (in Å/atom) associated with the JTD Q<sub>2</sub>-type mode in Ca<sub>2</sub>RuO<sub>4</sub> nanofilm in the ground state with octahedral rotations (left panels) and without O<sub>6</sub> group rotations (right panels). **c** Evolution of  $\Delta E_g$  as a function of the displacement  $u_{JTD}$  (in Å/atom) associated with the JTD

 $Q_2$  -type mode. The resulting Reduced Electron Phonon Matrix Element is estimated to D = 9.46 eV.Å $^{\rm -1}$ .d Total density of states (in states/eV/f.u/spin, grey area) as a function of the energy using the DFT calculation (lower part) and atomic-like Wannier functions (upper part). The WFs further allow to extract only contributions from the  $d_{xz}$  and  $d_{yz}$  orbitals (red line). The contribution from each  $d_{xz}$  or  $d_{yz}$  band is then of  $\mathcal{M}_F)$  = 0.31 states/eV/Ru/spin/band. The k-mesh is sampled with 12 x 12 x 4 points for the DFT calculation and with 256 x 256 x 64 points for the WFs. A ferromagnetic order is used throughout these calculations.

#### Outlook

In summary, ruthenates are proposed to be the first identified oxide materials showing superconductivity mediated by an electron-phonon coupling related to the proximity of orbital and bond ordering instabilities. This mechanism is in fact very similar to many other oxides reaching SC at the vicinity of a charge-ordered phase such as nickelates, bismuthates, or antimonates. The underpinning mechanism yielding SC in correlated oxides likely relates with coupled electron-phonon features—such as JTE and disproportionation effects—opening band gaps<sup>19</sup>. The global strategy to reach SC appears to sufficiently weaken these EPC to drive the material in a metallic regime albeit the EPC has to remain sufficiently large to mediate Cooper pairs formation.

#### Methods

# **Exchange-correlation functional**

We use the meta-Generalized Gradient Approximation (GGA) Strongly Constrained and Appropriately Normalized SCAN<sup>41</sup> functional that better amends self-interaction errors (SIE) inherent to practiced DFT over classical Local Density Approximation (LDA) and GGA functionals. This functional is able to predict the correct trends in lattice distortions and metal-insulator transitions in bulk ABO<sub>3</sub> perovskite oxides and trends in doping effects in nickelates, bismuthates and antimonates  $^{10,14,42,43}$ . In addition, SCAN does not require any external parameter as in DFT +  $\it U$ .

# **Magnetic orders**

We used several long-range magnetic orders such as a ferromagnetic (FM), A-type AFM (AFM-A) consisting of Ru spins coupled ferromagnetically in (ab)-planes and then coupled AFM along the  $\bf c$  axis and C-type AFM (AFM-C) with Ru spins coupled antiferromagnetically in the (ab)-plane. A paramagnetic (PM) calculation is also performed by using the special quasi-random structure (SQS) method to extract the Ru spin arrangement mimicking a PM state within a given supercell size<sup>19,44,45</sup>. It allows to get a snapshot of all possible local magnetic configurations (i.e., motifs) for Ru cations that would appear in a real PM phase. A 16 f.u corresponding to a  $(2\sqrt{2}, 2\sqrt{2}, 1)$  supercell with respect to the undistorted I4/mmm cell (2 f.u) is used for these simulations. Spins are only treated at the colinear level. The ATAT package is used for identifying the spin arrangement maximizing the disorder characteristic of a random spin configuration<sup>46</sup> within a given supercell size<sup>44</sup>. A non-spin

polarized calculation (NM) is also performed in which the number of electrons with a spin up and a spin down are force to be equal by construction on all Ru cations.

#### Crystallographic cells, structural relaxations, and analysis

The imposed starting cells correspond to high symmetry I4/mmm and the Pbca tetragonal unit cells for  $\rm Sr_2RuO_4^{47}$  and  $\rm Ca_2RuO_4^{25,33}$ , respectively.  $\rm Sr_2RuO_4$  exhibits only a small  $\rm a^0a^0c^+$  octahedral rotation while  $\rm Ca_2RuO_4$  exhibits large  $\rm a^-a^-c^+$   $\rm O_6$  group rotations induced by the usual A-to-B cation size mismatch. We proceed to the full structural relaxation (cell parameters and shape as well as atomic positions) until the forces acting on each atom are less than 0.005 eV/Å. Amplitude of the distortions of the relaxed ground states are then extracted using symmetry mode analysis taking as reference the undistorted I4/mmm cell. This is performed with the ISODISTORT tool from the ISOTROPY applications  $^{48,49}$ .

# Seeking for electronic instabilities

The SCAN functional is a local functional of the density matrix unable to make distinction between occupied and unoccupied states—unlike DFT + *U* or DFT with a hybrid functional. It is therefore unable to identify electronic instabilities in high symmetry cells with degenerate partners as performed in ref. 19 where one has to impose integer occupancy of a specific degenerate partner such as (1,0) instead of (0.5,0.5) for two degenerate orbitals. Instead, we used the strategy proposed in ref. 24: we plot the potential energy surface associated with a lattice distortion and seek to see the shape of the potential energy surface. A shifted single well potential whose minimum is located at non-zero amplitude of the mode then indicates the presence of an electronic instability as those observed for the Jahn-Teller or bond disproportionation distortions in ref. 24.

#### Potential energy surface and phonon frequencies

The potential energy surfaces associated with the Jahn-Teller  $Q_2$ -type distortion are computed by freezing different distortion amplitudes  $Q_{\rm JTD}$  in the material. This is done starting either from a highly symmetric I4/mmm to extract the propensity of the material to display a Jahn-Teller effect or from the ground state to extract the mode frequency. Due to the presence of potential electronic instabilities that move the single well minimum to non-zero amplitude of  $Q_{\rm ITD}$ , the evolution of the energy  $\Delta E$  is

given by the following expression:

$$\Delta E = E_0 + \alpha (Q_{\text{ITD}} - Q_0)^2 + \beta (Q_{\text{ITD}} - Q_0)^4$$
 (1)

where  $\alpha$  and  $\beta$  are coefficients and  $Q_0$  signals the force acting on the electrons even in the absence of  $Q_{JTD}$  (i.e., the electronic instability). It follows that

$$\Delta E = E_0 + \alpha Q_{\text{JTD}}^2 + \alpha Q_0^2 - 2\alpha Q_{\text{JTD}} Q_0 + \beta Q_{\text{JTD}}^4 + \beta Q_0^4 - 4\beta Q_{\text{JTD}}^3 Q_0 - 4\beta Q_{\text{JTD}} Q_0^3 + 6\beta Q_{\text{JTD}}^2 Q_0^2$$
(2)

$$\begin{split} \Delta E = & E_0 + \left(\alpha Q_0^2 + \beta Q_0^4\right) + (-2\alpha Q_0 - 4\beta Q_0^3) Q_{\rm JTD} + (\alpha + 6\beta Q_0^2) Q_{\rm JTD}^2 \\ & - 4\beta Q_0 Q_{\rm JTD}^3 + \beta Q_{\rm JTD}^4 \end{split} \tag{3}$$

$$\Delta E = E'_0 + aQ_{\text{ITD}} + bQ_{\text{ITD}}^2 + cQ_{\text{ITD}}^3 + dQ_{\text{ITD}}^4$$
 (4)

From Eq. 4, we recover the linear and trilinear terms in  $Q_{\rm JTD}$  signaling the contribution of the electronic instability. Using a fit of the potential energy surfaces as a function of  $Q_{\rm JTD}$  with a polynomial expression up to the 4<sup>th</sup> order, we can extract all coefficients of Eq.4 and map them to get the mode frequency through the relation  $\omega = \sqrt{\frac{2\pi}{4t}}$ .

As reported in several works on oxide perovskites  $^{20,37,38}$ ,  $a^0a^0c^+$  ( $\phi^+$ ) and  $a^*a^*c^0$  ( $\phi^-$ ) octahedral rotations possess a linear coupling with the JTD  $Q_2$ -type mode in the free energy expansion starting from the high symmetry undistorted cell:  $F \propto F'_0 + a'Q^2_{\text{JTD}} + b'Q^4_{\text{JTD}} + c'Q_{\text{JTD}} + d'Q^3_{\text{JTD}}$  where a', b', c' and d' are coefficients depending on the amplitude of octahedral rotations. By using the invariant module of the isotropy suite of software, we extract at the lowest order in amplitudes of the distortions that:

$$a' = a_{20} + a_{22}Q_{\phi^{-}}^{2} \tag{5}$$

$$b' = b_4 \tag{6}$$

$$c' = c_{110}Q_{\phi^+} + c_{130}Q_{\phi^+}^3 + c_{112}Q_{\phi^+}Q_{\phi^-}^2$$
 (7)

$$\mathbf{d}' = \mathbf{d}_{31} Q_{\Phi^+} \tag{8}$$

$$F'_{0} = F_{0} + e_{020}Q_{\phi^{+}}^{2} + e_{002}Q_{\phi^{-}}^{2} + e_{040}Q_{\phi^{+}}^{4} + e_{004}Q_{\phi^{-}}^{4} + e_{022}Q_{\phi^{-}}^{2}Q_{\phi^{-}}^{2}$$
(9)

Without octahedral rotations, one simply recovers the usual equation  $F \propto aQ_{\rm JTD}^2 + bQ_{\rm JTD}^4$ . The role of octahedral rotations is to tune the different coefficients, notably the a coefficient in front  $Q_{\rm JTD}^2$  that will drive the frequency of the mode. Using fits up to the  $4^{\rm th}$  order in  $Q_{\rm JTD}$ , one gets the frequency through the relation  $\omega = \sqrt{\frac{2a'}{M}}$ . We obtain fits with a coefficient of determination  $R^2$  of at least 0.9995 for our different potentials.

### **Superconducting properties**

We have calculated the reduced electron-phonon matrix element (REPME) associated with the JTD by freezing its atomic displacement in the structure. Using the band splitting amplitude  $\Delta E_{\rm g}$  appearing in the band structure in the first Brillouin zone due to the frozen phonon displacement, we compute the REPME by using the following formula  $D = \frac{\Delta E_{\rm g}}{2u}$ , where u is the displacement of one O atom for the condensed phonon mode. This standard procedure was successful in BaBiO<sub>3</sub>, SrBiO<sub>3</sub>, BaSbO<sub>3</sub>, or MgB<sub>2</sub> compounds<sup>10,11,14,50</sup>. In order to calculate the electron-phonon coupling  $\lambda$ , we use the following formula  $\lambda = N(E_{\rm F}) \frac{\hbar^2}{2M\omega^2} D^2$ , where  $N(E_{\rm F})$  is the density of states at the Fermi level per spin channel, formula unit and per contributing band, M is the

mass of the moving ion in the phonon mode and  $\omega_{JTD}$  is the frequency of the JT phonon mode. To obtain the critical temperature  $T_c$ , we use the McMillian-Allen equation<sup>39</sup>

$$T_{c} = \frac{\omega_{\log}}{1.2} \exp\left(\frac{-1.04(\lambda + 1)}{\lambda - \mu^{*}(1 + 0.62\lambda)}\right)$$
(10)

where  $\omega_{log}$  is the logarithmic averaged phonon frequency (expressed in K) and  $\mu^*$  is the screened Coulomb potential with conventional values ranging from 0.1 to 0.15. Since the JTD provides a significant contribution to the electron-phonon coupling, we impose that  $\omega_{log} = \omega_{JTD}$  for estimating  $T_c$ . We used the FM order to compute the superconducting properties since local spin formation is critical for quantifying SC in correlated oxides<sup>12</sup>. Such FM order is suggested experimentally in Sr<sub>2</sub>RuO<sub>4</sub> and observed in the superconducting of Ca<sub>2</sub>RuO<sub>4</sub> nanofilm<sup>32,34,51</sup>.

#### Density of states at $E_{\rm F}$

In order to have accurate density of states at the Fermi level, we have employed the wannier90 package  $^{52-55}$  on top of our electronic structure calculations. To that end, we have built the Wannier functions associated with the three  $t_{2g}$  bands of Ru cations in the minority spin channel. We have projected the 12 Kohn-Sham states located around the Fermi level (4 Ru cations times 3 d states) on  $d_{xy}$ ,  $d_{xz}$ , and  $d_{yz}$  guess orbitals centered on Ru cations. After the wannierization, we end up with 12 well-defined  $d_{xy}$ ,  $d_{xz}$ , and  $d_{yz}$  atomic-like Wannier functions centered on each Ru cation. Using these WFs, we then proceed to the calculation of the density of states (dos) on a very large kmesh consisting of  $256\times256\times64$  k points. We checked carefully that the dos matched the initial DFT dos computed on a smaller kmesh of  $12\times12\times4$  k points. Furthermore, the WFs allow to extraction the contribution of  $d_{xz}$  and  $d_{yz}$  orbitals to the density of state at the Fermi level  $N(E_{\rm F})$  since only these bands contribute to the SC properties.

#### Other technical details

DFT simulations are performed with the Vienna Ab initio Simulation Package (VASP) $^{56,57}$ . Projector Augmented Wave pseudo potentials $^{58}$  (PAW) are used taking the  $5s^24d^6$ ,  $4s^24p^65s^2$ ,  $3s^23p^64s^2$ , and  $2s^22p^4$  as valence electrons for Ru, Sr, Ca, and O atoms, respectively. The energy cut-off is set to 650 eV and is accompanied by a  $8\times8\times4$  ( $4\times4\times2$ ) Gamma centered k-mesh for the structural relaxations with long-range magnetic orders (PM order). It is further increased to  $12\times12\times4$  for calculations of density of states with VASP. Band structures are unfolded to the primitive I4/mmm cell using the VaspBandUnfold package.

#### Data availability

The data supporting this research is openly available from ref. 59.

# Code availability

VASP DFT code license can be purchased from Vienna University.

#### References

- Keimer, B., Kivelson, S. A., Norman, M. R., Uchida, S. & Zaanen, J. From quantum matter to high-temperature superconductivity in copper oxides. *Nature* 518, 179–186 (2015).
- Cooper, L. N. Bound electron pairs in a degenerate fermi gas. *Phys. Rev.* 104, 1189 (1956).
- Maeno, Y. et al. Superconductivity in a layered perovskite without copper. Nature 372, 532–534 (1994).
- Kim, M. et al. Superconductivity in (Ba,K)SbO<sub>3</sub>. Nat. Mater. 21, 627–633 (2022).
- Sleight, A. W., Gillson, J. L. & Bierstedt, P. E. High-temperature superconductivity in the BaPb<sub>1-x</sub>Bi<sub>x</sub>O<sub>3</sub> system. Solid State Commun. 17, 27 (1975).

- Kazakov, S. M. et al. Discovery of a second family of bismuth-oxidebased superconductors. *Nature* 390, 148–150 (1997).
- Li, D. et al. Superconductivity in an infinite-layer nickelate. Nature 572, 624–627 (2019).
- 8. Pan, G. A. et al. Superconductivity in a quintuple-layer square-planar nickelate. *Nat. Mater.* **21**, 160 (2021).
- Sun, H. et al. Superconductivity near 80 Kelvin in single crystals of La<sub>3</sub>Ni<sub>2</sub>O<sub>7</sub> under pressure. *Nature* 621, 493 (2023).
- Varignon, J. Origin of superconductivity in hole doped SrBiO<sub>3</sub> bismuth oxide perovskite from parameter-free first-principles simulations. NPJ Comput Mater. 9, 30 (2023).
- Yin, Z. P., Kutepov, A. & Kotliar, G. Correlation-enhanced electronphonon coupling: Applications of GW and screened hybrid functional to bismuthates, chloronitrides, and other high-T<sub>c</sub> superconductors. *Phys. Rev. X* 3, 021011 (2013).
- Carrasco Álvarez, Á. A. et al. Charge ordering as the driving mechanism for superconductivity in rare-earth nickel oxides. *Phys. Rev. Mater.* 8, 064801 (2024).
- Carrasco Álvarez, Á. A. et al. Electron-phonon mediated superconductivity in La<sub>6</sub>Ni<sub>5</sub>O<sub>12</sub> nickel oxides. *Phys. Rev. B* 110, 235107 (2024).
- Varignon, J. Decisive role of hybridized electronic states on the appearance of superconductivity in Ba<sub>1-x</sub>K<sub>x</sub>MO<sub>3</sub> (M=Bi, Sb). *Phys. Rev. B* 110, 125120 (2024).
- Zhao, H. et al. Cascade of correlated electron states in the kagome superconductor CsV<sub>3</sub>Sb<sub>5</sub>. Nature 599, 216–221 (2021).
- Li, L. et al. Superconducting order from disorder in 2H-TaSe<sub>2-x</sub>S<sub>x</sub>. NPJ Quantum Mater. 2, 11 (2017).
- Kusmartseva, A. F., Sipos, B., Berger, H., Forró, L. & Tutiš, E. Pressure induced superconductivity in pristine 1T-TiSe<sub>2</sub>. Phys. Rev. Lett. 103, 236401 (2009).
- Koley, S., Mohanta, N. & Taraphder, A. Charge density wave and superconductivity in transition metal dichalcogenides. *Eur. Phys. J.* B 93, 77 (2020).
- Varignon, J., Bibes, M. & Zunger, A. Origin of band gaps in 3d perovskite oxides. *Nat. Commun.* 10, 1658 (2019).
- Varignon, J., Bibes, M. & Zunger, A. Origins vs. fingerprints of the Jahn-Teller effect in d-electron ABX<sub>3</sub> perovskites. *Phys. Rev. Res.* 1, 033131 (2019).
- Jahn, H. A. & Teller, E. Stability of polyatomic molecules in degenerate electronic states. I. Orbital degeneracy. Proc. R. Soc. Lond. A Math. Phys. Sci. 161, 220–235 (1937).
- Miyasaka, S., Okimoto, Y., Iwama, M. & Tokura, Y. Spin-orbital phase diagram of perovskite-type RVO<sub>3</sub> (R= rare-earth ion or Y). *Phys. Rev.* B 68, 100406 (2003).
- Kugel, K. I. & Khomskii, D. I. Crystal-structure and magnetic properties of substances with orbital degeneracy. Sov. Phys. JETP 64, 1429–1439 (1973).
- Varignon, J., Malyi, O. I. & Zunger, A. Dependence of band gaps in d
  -electron perovskite oxides on magnetism. *Phys. Rev. B* 105,
  165111 (2022).
- 25. Friedt, O. et al. Structural and magnetic aspects of the metal-insulator transition in Ca<sub>2-x</sub>Sr<sub>x</sub>RuO<sub>4</sub>. *Phys. Rev. B* **63**, 1744321 (2001).
- 26. Martínez, J. L. et al. Structural and magnetic properties of  $Sr_2RuO_4$ -type oxides. J. Magn. Magn. Mater. **140–144**, 179–180 (1995).
- 27. Glazer, A. M. The classification of tilted octahedra in perovskites. *Acta Crystallogr. B* **28**, 3384 (1972).
- Alexander, C. S. et al. Destruction of the Mott insulating ground state of Ca<sub>2</sub>RuO<sub>4</sub> by a structural transition. *Phys. Rev. B* 60, R8422–R8425 (1999).
- Georgescu, A. B. & Millis, A. J. Quantifying the role of the lattice in metal-insulator phase transitions. *Commun. Phys.* 5, 135 (2022).
- 30. Nakatsuji, S. et al. Mechanism of hopping transport in disordered mott insulators. *Phys. Rev. Lett.* **93**, 146401 (2004).

- Maeno, Y., Rice, T. M. & Sigrist, M. The intriguing superconductivity of strontium ruthenate. *Phys. Today* 54, 42–47 (2001).
- Nobukane, H. et al. Co-appearance of superconductivity and ferromagnetism in a Ca<sub>2</sub>RuO<sub>4</sub> nanofilm crystal. Sci. Rep. 10, 3462 (2020).
- Braden, M. & André, G. Crystal and magnetic structure of magnetoelastic coupling and the metal-insulator transition. *Phys. Rev. B* 58, 847–861 (1998).
- 34. Ortmann, J. E. et al. Competition between antiferromagnetism and ferromagnetism in Sr<sub>2</sub>RuO<sub>4</sub> probed by Mn and Co doping. *Sci. Rep.* **3**, 2950 (2013).
- 35. Huang, H. L. & Jeng, H. T. Orbital ordering and magnetism in layered Perovskite Ruthenate Sr<sub>2</sub>RuO<sub>4</sub>. Sci. Rep. **10**, 7089 (2020).
- Schmitt, M. M., Zhang, Y., Zhang, Y., Mercy, A. & Ghosez, P. Electron-lattice interplay in LaMnO<sub>3</sub> from canonical Jahn-Teller distortion notations. *Phys. Rev. B* 101, 214304 (2020).
- 37. Varignon, J., Bristowe, N. C., Bousquet, E. & Ghosez, P. Coupling and electrical control of structural, orbital and magnetic orders in perovskites. *Sci. Rep.* **5**, 15364 (2015).
- 38. Varignon, J., Grisolia, M. N., Preziosi, D., Ghosez, P. & Bibes, M. Origin of the orbital and spin ordering in rare-earth titanates. *Phys. Rev. B* **96**, 235106 (2017).
- 39. Allen, P. B. & Dynes, R. C. Transition temperature of d-f-band superconductors. *Phys. Rev. B* **12**, 905 (1975).
- Mercy, A., Bieder, J., Íñiguez, J. & Ghosez, P. Structurally triggered metal-insulator transition in rare-earth nickelates. *Nat. Commun.* 8, 1677 (2017).
- Sun, J., Ruzsinszky, A. & Perdew, J. Strongly constrained and appropriately normed semilocal density functional. *Phys. Rev. Lett.* 115, 036402 (2015).
- Varignon, J., Bibes, M. & Zunger, A. Mott gapping in 3d ABO<sub>3</sub> perovskites without Mott-Hubbard interelectronic repulsion energy U. *Phys. Rev. B* 100, 035119 (2019).
- Iglesias, L., Bibes, M. & Varignon, J. First-principles study of electron and hole doping effects in perovskite nickelates. *Phys. Rev. B* 104, 035123 (2021).
- 44. Zunger, A., Wei, S.-H., Ferreira, L. G. & Bernard, J. E. Special quasirandom structures. *Phys. Rev. Lett.* **65**, 353 (1990).
- Trimarchi, G., Wang, Z. & Zunger, A. Polymorphous band structure model of gapping in the antiferromagnetic and paramagnetic phases of the Mott insulators MnO, FeO, CoO, and NiO. *Phys. Rev. B* 97, 035107 (2018).
- 46. Van de Walle, A., Asta, M. & Ceder, G. The alloy theoretic automated toolkit: A user guide. *CALPHAD* **26**, 539–553 (2002).
- Huang, Q. et al. Neutron Powder diffraction study of the crystal structures of Sr<sub>2</sub>RuO<sub>4</sub> and Sr<sub>2</sub>IrO<sub>4</sub> at room temperature and at 10 K. J. Solid State Chem. 112, 355 (1998).
- Campbell, B. J., Stokes, H. T., Tanner, D. E. & Hatch, D. M. ISODIS-PLACE: a web-based tool for exploring structural distortions. *J. Appl Crystallogr.* 39, 607–614 (2006).
- 49. ISOTROPY Software Suite, iso.byu.edu. https://iso.byu.edu/iso/isodistort\_version5.6.1/isodistort.php.
- 50. An, J. M. & Pickett, W. E. Superconductivity of MgB<sub>2</sub>: covalent bonds driven metallic. *Phys. Rev. Lett.* **86**, 4366–4369 (2001).
- 51. Minakata, M. & Maeno, Y. Magnetic ordering in Sr<sub>2</sub>RuO<sub>4</sub> induced by nonmagnetic impurities. *Phys. Rev. B* **63**, 180504(R) (2001).
- Mostofi, A. A. et al. Wannier90: a tool for obtaining maximally-localised Wannier functions. *Comput. Phys. Commun.* 178, 685–699 (2008).
- Marzari, N. & Vanderbilt, D. Maximally localized generalized Wannier functions for composite energy bands. *Phys. Rev. B* 56, 12847 (1997).
- Souza, I., Marzari, N. & Vanderbilt, D. Maximally localized Wannier functions for entangled energy bands. *Phys. Rev. B* 65, 35109 (2001).
- 55. Pizzi, G. et al. Wannier90 as a community code: new features and applications. *J. Phys. Condens. Matter* **32**, 165902 (2020).

- Kresse, G. & Haffner, J. Ab initio molecular dynamics for liquid metals. *Phys. Rev. B* 47, 558 (1993).
- 57. Kresse, G. & Furthmüller, J. Efficiency of ab-initio total energy calculations for metals and semiconductors using a plane-wave basis set. *Comput Mater. Sci.* **6**, 15 (1996).
- 58. Blöchl, P. E. Projector augmented-wave method. *Phys. Rev. B* **50**, 17953 (1994).
- 59. Carrasco Álvarez, Á. A. et al. Data archive available on Figshare. https://doi.org/10.6084/m9.figshare.28108970.

# **Acknowledgements**

This work has received financial support from the CNRS through the MITI interdisciplinary programs under the project SuNi. J.V. acknowledges support from the Région Normandie through the CPER project "PROPRE". Authors acknowledge access granted to HPC resources of Criann through the projects 2020005 and 2007013 and of Cines through the DARI project A0080911453.

# **Author contributions**

The project was conceived by J.V., M.B., and W.P. J.V. designed and directed the study. A.A.C.A. and J.V. performed the electronic structure calculations with support from S.P. J.V. and A.A.C.A performed the analysis with help from all co-authors. J.V. and A.A.C.A wrote the manuscript with inputs from all co-authors.

# **Competing interests**

The authors declare no competing interests.

### **Additional information**

**Supplementary information** The online version contains supplementary material available at https://doi.org/10.1038/s41467-025-56417-5.

**Correspondence** and requests for materials should be addressed to Julien Varignon.

**Peer review information** *Nature Communications* thanks G. Lucian Pascut, and the other, anonymous, reviewer for their contribution to the peer review of this work. A peer review file is available.

**Reprints and permissions information** is available at http://www.nature.com/reprints

**Publisher's note** Springer Nature remains neutral with regard to jurisdictional claims in published maps and institutional affiliations.

Open Access This article is licensed under a Creative Commons Attribution-NonCommercial-NoDerivatives 4.0 International License, which permits any non-commercial use, sharing, distribution and reproduction in any medium or format, as long as you give appropriate credit to the original author(s) and the source, provide a link to the Creative Commons licence, and indicate if you modified the licensed material. You do not have permission under this licence to share adapted material derived from this article or parts of it. The images or other third party material in this article are included in the article's Creative Commons licence, unless indicated otherwise in a credit line to the material. If material is not included in the article's Creative Commons licence and your intended use is not permitted by statutory regulation or exceeds the permitted use, you will need to obtain permission directly from the copyright holder. To view a copy of this licence, visit <a href="https://creativecommons.org/licenses/by-nc-nd/4.0/">https://creativecommons.org/licenses/by-nc-nd/4.0/</a>.

© The Author(s) 2025